Search for the Jacobi shape transition in rapidly rotating nuclei

D. Ward,[1] R. M. Diamond,[1] W. J. Swiatecki,[1] R. M. Clark,[1] M. Cromaz,[1] M. A. Deleplanque,[1] P. Fallon,[1] A. Goergen,[1] G. J. Lane,[1,2] I. Y. Lee,[1] A. O. Macchiavelli,[1] W. Myers,[1] F. S. Stephens,[1] C. E. Svensson,[1,3] and K. Vetter[1,4]

[1]*Nuclear Science Division, Lawrence Berkeley National Laboratory, Berkeley, California 94720*

[2]*Department of Nuclear Physics, Research School of Physical Sciences and Engineering, Australian National University, Canberra ACT 0200, Australia*

[3]*Department of Physics, University of Guelph, Guelph, Ontario, Canada N1G 2W1*

[4]*Glenn T. Seaborg Institute, Lawrence Livermore National Laboratory, Livermore, California 94550*

(Received 23 April 2002; published 23 August 2002)

We have studied quasicontinuous gamma radiation from reactions of ^{48}Ca beams on targets of ^{50}Ti, ^{64}Ni, ^{96}Zr, and ^{124}Sn. The bombarding energies were in the range 195–215 MeV, and were chosen so as to bring in a high angular momentum without severe fragmentation of the cross sections for fusion residues. Experiments were performed both with the 8PI spectrometer at the LBNL 88-Inch Cyclotron, and with Gammasphere at the ANL ATLAS accelerator. The results have been analyzed in a variety of ways, with the consistent result that in all but the heaviest target, the nuclear moments of inertia tend to increase with increasing angular momentum up to the highest values observed. This could come from a transition towards a highly deformed Jacobi-like shape, or possibly be due to the appearance of high-j intruder orbitals at the Fermi surface. We will argue that these effects can be equivalent.

DOI: 10.1103/PhysRevC.66.024317 PACS number(s): 21.60.−n, 21.60.Ev

I. INTRODUCTION

It is a general property of rotating classical fluids that beyond a certain critical angular momentum L_1, the equilibrium shape changes abruptly from a slightly flattened configuration to a triaxial shape rotating about its shortest axis. With increasing angular momentum, this configuration elongates very rapidly and eventually fissions at a characteristic angular momentum L_2.

The original discovery of such a transition from oblate to triaxial shapes was made in 1834 by Jacobi, in the context of rotating, idealized, incompressible, gravitating masses. In 1961, Beringer and Knox [1] suggested that a similar transition might be expected in the case of atomic nuclei, idealized as incompressible, uniformly charged, liquid drops endowed with surface tension. Subsequent theoretical studies in 1974 and in 1986 [2] confirmed this conjecture. It was also realized that the mathematical problem of a rotating, uniformly charged drop goes over smoothly into Jacobi's classic astronomical problem by making the magnitude of the repulsive electrostatic energy decrease through zero to negative values, at which point it becomes a Newtonian attraction [3].

In 1996, the oblate-to-triaxial transition was found to take place in the more realistic nuclear Thomas-Fermi model under the assumption of synchronous rotation, i.e., that all mass elements rotate with a common angular velocity [4]. The Thomas-Fermi model is a self-consistent, mean-field, semiclassical solution of the problem of nucleons interacting through finite-range forces. It gives a good description of average static nuclear properties such as binding energies and fission barriers, but nuclear shell effects are not taken into account. Shell effects can produce sharp deviations from average binding energies (and shapes) and, moreover, the assumption of synchronous rotation is known to be strongly violated at low angular momenta where pairing effects are important.

Conventional superdeformed nuclei owe their elongation to shell effects, and are observed down to relatively low angular momenta (spin zero in some fission isomers). By contrast, the existence of Jacobi-like configurations is due to the centrifugal force, and, without help from shell effects, such shapes would appear only at very high angular momentum; but they should then occur over a wider range of nuclei rather than in the small pockets characteristic of the effects driven by shell structure.

Evidence for Jacobi effects must be sought in the quasicontinuous γ spectrum emitted from states of very high angular momentum. For example, Maj *et al.* [5] have recently presented evidence for a Jacobi transition in ^{46}Ti, based on the analysis of the γ spectrum associated with decays of the giant-dipole resonance. In this paper we will present experimental indications that strongly elongated nuclei, reminiscent of the Jacobi configurations, are produced in reactions resulting from the bombardment of ^{50}Ti, ^{64}Ni, ^{96}Zr targets with beams of ^{48}Ca. The effect occurs at a lower angular momentum than a ''classical'' Jacobi transition, and appears to be gradual rather than sharp. In the case of the ^{124}Sn target, there is no evidence yet for such a transition in the spin region observed.

II. EXPERIMENT

At Lawrence Berkeley National Laboratory, targets of ^{64}Ni and ^{124}Sn were bombarded with beams of ^{48}Ca delivered by the 88-Inch Cyclotron. Target characteristics and bombarding energies are given in Table I. Gamma rays were detected in the 8PI spectrometer [6], which comprises an outer array of 20 Compton-shielded HPGe detectors, and an inner array, or ball, of 71 bismuth germanate (BGO) scintillation detectors. This inner array covers a solid angle of $\approx$94% of 4π steradians, and has very good multiplicity M resolution. Its response, that is, the number of BGO ball

TABLE I. Summary of the experimental conditions. The calculation of L_{max} assumes fusion at grazing incidence with $R_0 = 1.2$ F.

Target	Thickness (mg)	Incident energy (MeV)	Calculated L_{max} ($\hbar$)	Events (8PI)	Events (Gammasphere)
^{50}Ti	0.5	200	70	0	1.9×10^{9}
^{64}Ni	(0.4)+(0.38)	207	79	3.5×10^{8}	2.1×10^{9}
^{96}Zr	1.0	207	86	0	2.2×10^{9}
^{124}Sn	(0.44)+(0.44)	215	88	4.5×10^{7}	9.0×10^{8}

elements that fire (K) on being presented with a given input γ-ray multiplicity has been determined with radioactive sources according to the method described by Jääskelainen *et al.* [7].

At Argonne National Laboratory, targets[1] of ^{50}Ti, ^{64}Ni, ^{96}Zr, and ^{124}Sn were bombarded with ^{48}Ca beams delivered by the ATLAS accelerator. Gamma rays were detected in the Gammasphere array [8]. In order to achieve the best possible response in K, the ''hevimet'' pieces that usually shield the Compton suppressors from a direct view of the target were removed. This increased the rate of false veto signals, and the efficiency of the instrument was reduced by as much as a factor of 2, but it provided an efficient measurement of the γ-ray multiplicity of a quality comparable to that obtained from the 8PI spectrometer described above. In Gammasphere, the fold K is defined as the number of modules that detected a γ ray, where a module is defined as an HPGe detector and its associated suppression shields (actually seven separate BGO detectors). Gammasphere contains up to 108 HPGe/BGO modules. We define K as the number of modules which have been hit at least once. For example, a hit on an HPGe detector and one or more of its shields is counted as one hit module and contributes one count to the K value.

The response functions in K measured for Gammasphere with a ^{60}Co source are shown in Fig. 1. These differ little from the corresponding functions for the 8PI spectrometer. For moderate γ-ray multiplicities M, Gammasphere typically registers two more hits than the 8PI spectrometer. We believe that this is because there is more scattering between detectors where the BGO pieces are rather thin, near the apices of the Gammasphere suppression shields. At very high multiplicity, say M greater than 40, where the multiplicity of γ rays begins to become significant relative to the number of detectors (71) in the 8PI spectrometer, Gammasphere registers typically four more hits than the 8PI spectrometer. This increase comes about because there are more detectors in Gammasphere than in the 8PI spectrometer, so that the number of multiple hits on one element are fewer.

In the Gammasphere experiments, events were written to tape on a trigger of five Compton-suppressed coincident HPGe hits. The information written included the participating HPGe energies and times, together with the associated H and K values computed by the Gammasphere data acquisition program. Here, H is the total detected γ-ray energy obtained by summing the outputs of all detectors registering in the event. Individual BGO parameters were not written. The timing requirement for including a hit in the H and K computation was that it be within ± 40 ns of the prompt time peak.

In the 8PI spectrometer experiments, the trigger was generally two Compton-suppressed coincident HPGe hits together with a minimum of seven ($K=7$) hits on the BGO ball. Some data were taken requiring only a single HPGe hit (with seven BGO hits). The data stream to tape included the participating HPGe energies and times, together with the associated H and K values computed in the data acquisition program [9]. The time requirement for including a hit in H and K was more restrictive than in the Gammasphere experiments, and was typically within ± 20 ns of the prompt time peak.

III. RESULTS

Our objective is to study γ spectra emitted by states of high angular momentum. Ideally we would like to isolate the

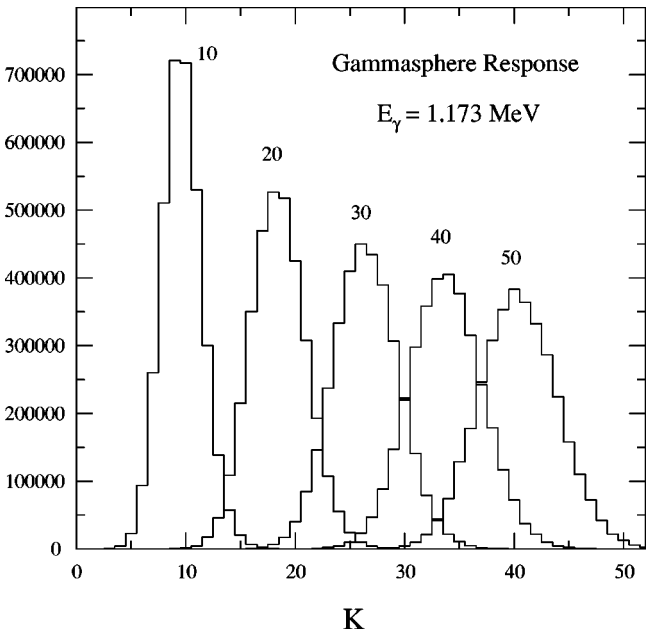

FIG. 1. Measured response functions for Gammasphere, $f_M(K)$, as described in the text. K is the fold, defined as the number of hit modules observed for the γ-ray multiplicity shown above the curves. The ''hevimet'' shielding over the Compton suppressors was removed.

[1]The same ^{64}Ni and ^{124}Sn targets were used at both laboratories.

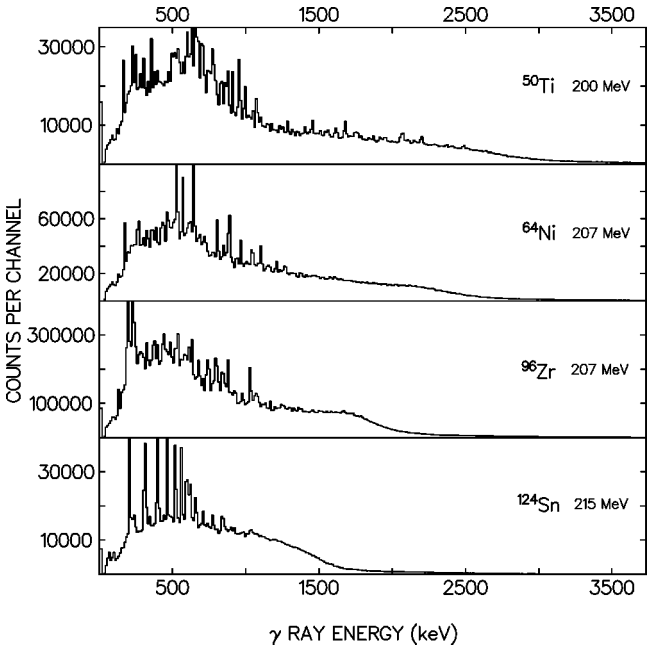

FIG. 2. Unprocessed HPGe spectra gated on $K=36$ obtained with Gammasphere for the ^{48}Ca reactions specified. A characteristic edge is present in all the spectra (e.g., at $\approx$2750, 2400, 1900, and 1400 keV for the targets ^{50}Ti, ^{64}Ni, ^{96}Zr, and ^{124}Sn, respectively) and gives a measure of the nuclear moment of inertia at the angular momentum selected by the K value.

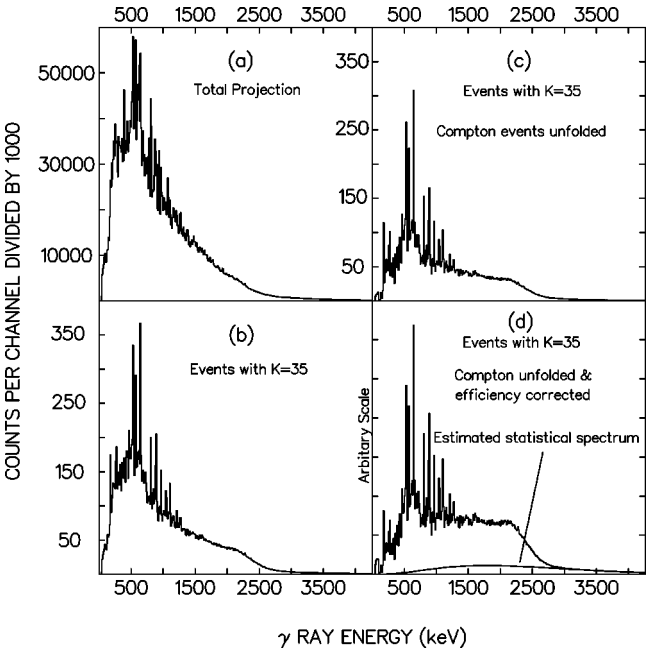

FIG. 3. Steps in the processing of the HPGe spectra. The data are for the ^{64}Ni target at 207 MeV, measured with Gammasphere.

average spectrum associated with transitions from states of a specific spin, I. What we did obtain was the γ spectrum associated with a specific range of spins by subtracting spectra gated in coincidence with neighboring folds, say K-1 or K-2 from that of K. These spectra have to be unfolded for Compton events, corrected for detector efficiency, and properly normalized. From the measured response function of the instrument, that is, the relationship between an input event multiplicity M and the corresponding output response K, we can then associate a range of M values with the subtracted, or incremental, spectrum. Finally, by measuring the angular distributions of γ rays about the beam axis, which to a good approximation leads to the average angular momentum removed per γ ray, we can associate an average spin value with the derived M value.

A. Processing the spectra

The data tapes were replayed into matrices with K on one axis and HPGe energy on the other. From these matrices, we projected HPGe spectra associated with individual K values. Examples of raw HPGe spectra are shown in Fig. 2. Each HPGe spectrum was processed by contracting the dispersion to 32/3 keV per channel, and then unfolding out Compton events. The response function was represented in an approximate way as a platform and a full-energy peak, the latter taken as one channel with a high count. The ratio of the platform height to the height of the single high channel simulating the photopeak was adjusted to the measured photopeak-to-total ratio and was represented by an analytic formula as a function of γ-ray energy. One small but necessary refinement was to linearly taper away the counts in the platform down to zero intensity over the region $E_\gamma \approx 200$ keV to $E_\gamma=0$. This is an obvious feature in the Gammasphere calibration spectra, and is caused by the diminishing efficiency of the constant-fraction discriminator for low-amplitude pulses. Failure to take this into account results in an oversubtraction of the spectra at low γ-ray energies. The effects of unfolding the Compton events are illustrated in Fig. 3, which shows data for the ^{64}Ni target.

The final steps in processing the spectra were to divide by the measured photopeak efficiency response, and to normalize the spectrum integral to the derived γ-ray multiplicity.

For some purposes, we found it convenient to subtract the statistical component of the spectrum. This was done by fitting the exponential fall of the high-energy tail in the spectrum to the function [10]

$$N(E_\gamma) \sim E_\gamma^3 \exp(-E_\gamma/T_{eff}), \tag{1}$$

where T_{eff} is an effective temperature. These steps are also illustrated in Fig. 3.

B. Anisotropy of the γ radiation

Angular distributions of γ rays with respect to the beam direction were obtained from samples of the Gammasphere data for each reaction. The data tapes were replayed to generate angle-dependent K matrices of HPGe spectra separated into the rings of common polar angles about the beam axis. From these matrices, histograms were generated by gating over narrow ranges in K selected at low, medium, and high multiplicity for each reaction. The spectra were unfolded to remove the Compton background, and anisotropy spectra were generated by dividing point by point the histogram from the ring at $\theta=163°$ by that for the ring at $\theta=90°$. Two

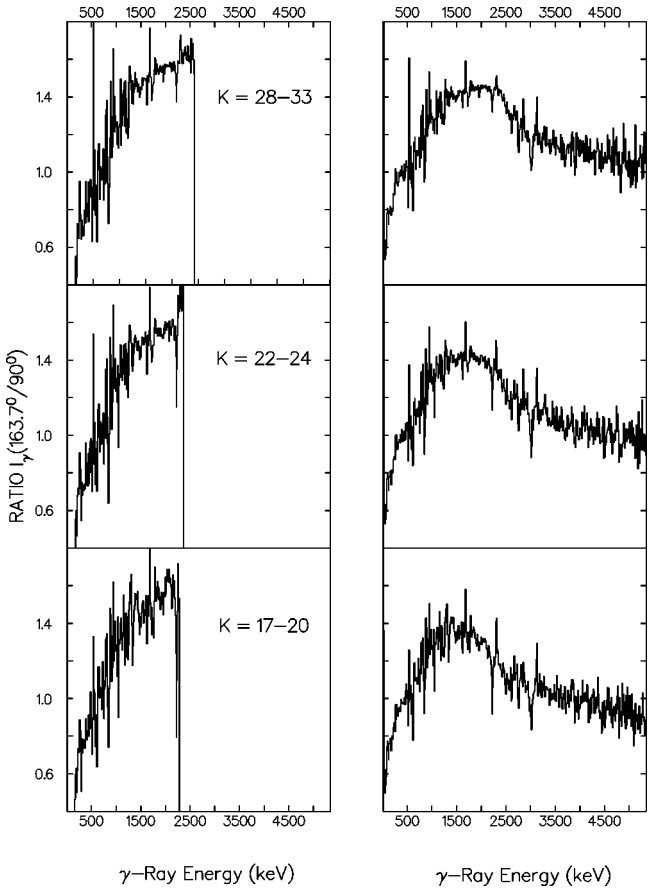

FIG. 4. Gamma-ray anisotropy spectra measured in Gammasphere for reactions on the ^{64}Ni target. In the left-hand panels, statistical transitions have been subtracted as described in the text. The right-hand panels refer to the raw spectra. The anisotropy cannot be extracted in the statistical region in spectra with the statistical transitions subtracted (left-hand panels), and this region is not shown.

sets of spectra were examined, with the division performed both before and after subtraction of the statistical component (as described above). Corrections for the measured relative detection efficiency of the rings, and for the relativistic aberration of the solid angle for emission from the recoiling nucleus were introduced. Examples for reactions on the ^{64}Ni target are shown in Fig. 4.

C. Decomposition of the spectra, and the angular momentum removed by the cascade

From the anisotropy spectra after subtraction of the statistical component, we made a simple decomposition of the spectra into $\Delta I=2$, $\lambda=2$ (stretched quadrupole transitions) and $\Delta I=1$, $\lambda=1$ (stretched dipole transitions). There may be other weak components, e.g., nonstretched transitions, mixed transitions, $\lambda=3$ transitions, etc., but it is not possible to reliably decompose the spectrum into more than the two basic components.

We take attenuation coefficients $\alpha_2=0.85$ and $\alpha_4=0.6$ as typical for the nuclear spin alignment, which for the angle ratio $R_\gamma=(163°/90°)$ gives $R_\gamma\sim1.55$ for stretched quadrupoles, and $R_\gamma\sim0.65$ for stretched dipoles [11]. As can be seen in Fig. 4 for the ^{64}Ni target, these values correspond to an assignment of $\approx100\%$ stretched $E2$ at the peak of the bump region and to a $\approx100\%$ stretched dipole at the lowest γ-ray energies. In fact, all four of the reactions studied ranged over a similar set of values.

TABLE II. Decomposition of spectral components and the angular momentum carried by the γ-ray cascade.

Target		Multiplicity				Ang. mom. ($\hbar$)
		Quad.	Dipole	Statistical	Total	
^{50}Ti						
	Low	5.9	9.2	3.9	19.0	23.3
	Medium	8.5	10.4	6.0	24.9	31.1
	High	12.8	11.1	8.0	31.9	41.9
^{64}Ni						
	Low	10.3	6.3	2.7	19.3	28.7
	Medium	13.7	6.8	3.3	23.8	36.3
	High	17.2	8.5	4.7	30.4	46.0
^{96}Zr						
	Low	7.0	10.2	4.2	21.4	26.9
	Medium	12.1	12.9	5.1	30.1	40.4
	High	14.5	15.4	5.9	35.8	48.2
^{124}Sn						
	Low	11.0	4.0	4.1	19.1	28.7
	Medium	17.2	3.6	5.2	26.0	41.4
	High	20.6	4.6	6.4	31.6	50.0

The spectra were decomposed into stretched quadrupole (SQ) and stretched dipole (SD) components as

$$I_{SQ}=I_\gamma(R_\gamma-R_{SD})/(R_{SQ}-R_{SD}), \tag{2}$$

$$I_{SD}=I_\gamma-I_{SQ}. \tag{3}$$

Operating on the multiplicity-normalized spectra, we then assigned multiplicities to the stretched quadrupole, stretched dipole, and statistical components as shown in Table II. Assuming that the near isotropy of the statistical spectrum arises from there being $\approx65\%$ $\Delta L=1$ dipoles and 35% $\Delta L=0$ dipoles, the angular momentum removed by the statistical cascade is $0.65\hbar$ times its multiplicity. The total angular momentum of the cascade for all the reactions and at three typical multiplicities is summarized in Table II.

Previous workers, e.g., [12], have suggested that an empirical relationship between the angular momentum carried by a γ-ray cascade, I, to the multiplicity M has the form

$$I=a(M-c), \tag{4}$$

where the constants a and c are determined by the data. Applying least-squares fits to the data shown in Table II shows that $c=3$ gives a good fit to all the data, and the derived values for a are given in Table III.

D. Multiplicity spectra

The K-spectra measured in the Gammasphere experiments are shown in Fig. 5. The corresponding multiplicity spectra

TABLE III. Relationship between angular momentum and multiplicity. The best fit to the results given in Table II expressed in the form $L=\text{coeff.}\times(M-3)\hbar$, where L is the angular momentum and M the multiplicity.

Target	Coefficient
^{50}Ti	1.44
^{64}Ni	1.73
^{96}Zr	1.48
^{124}Sn	1.78

were obtained by deconvoluting with the measured response functions, examples of which are shown in Fig. 1. In practice, this was achieved by convoluting trial M spectra with the response functions, and by iterating until the calculated K spectrum agreed closely with that measured. The calculated K spectrum was given by

$$N_K=\sum_{M=1,50} N_M f_M(K), \tag{5}$$

where $f_M(K)$ are the set of response functions, cf. Fig. 1, which we parametrized as Gaussians in the variable K, with a centroid and standard deviation fitted to the measured values as functions of the multiplicity M. The quantities N_M and N_K are the spectral intensities at the values K and M, respectively.

The multiplicity spectra shown in Fig. 5 are not at all like the true multiplicity spectra of the reaction: they were obtained with a trigger condition of five clean HPGe hits, and this heavily biases the detection efficiency against low-multiplicity events. We could of course take out the trigger bias, but we have not done so because this bias enters into all later aspects of the analysis equally, and does not affect the final results.

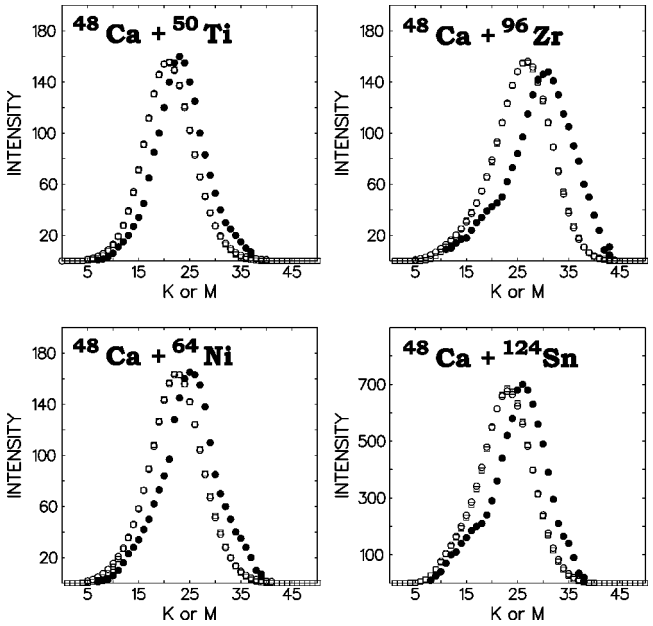

FIG. 5. Examples of derived multiplicity spectra (filled circles) for the four reactions measured in Gammasphere (see text). The measured K spectra are shown as open circles, and the K spectra calculated by convoluting the multiplicity spectra with the response functions are shown as open squares.

Multiplicity spectra obtained with the 8PI spectrometer were analyzed in the same way, using the appropriate response functions. The trigger condition in the 8PI experiments was much more transparent to low-multiplicity events. For example, in the case of the ^{48}Ca on ^{124}Sn reaction recorded with the 8PI spectrometer there is an intense peak at $\approx M=14$, which arises from fission reactions: the corresponding feature in the Gammasphere data can be seen in Fig. 5 as a small inflection on the low-multiplicity side of the multiplicity distribution.

From the relationship of N_M to N_K discussed above, we can compute the distributions $f_K(M)$, which express the M content projected out by a single K value; these distributions may be regarded as the inverse of the distributions $f_M(K)$ shown in Fig. 1. The $f_K(M)$ distributions have built into them the M spectrum specific to the measurement, as seen through a particular trigger bias. Generally, we have taken the M centroid of these distributions to be the average M associated with the experimental K selection.

E. Extraction of incremental γ spectra

By comparing the processed HPGe spectra for successively higher K values, we can, in effect, isolate the spectrum of γ-rays depopulating states of the very highest spins, that is, the transitions feeding in at the top of the γ cascade. The way to do this is to subtract the spectrum gated on K from that gated on $K+1$ with some normalization. We have explored various procedures for choosing the normalization. For example, the normalization could be chosen so as to cancel some region of the spectrum known to remain closely unchanged with the increasing K value; this could be the statistical component, or the region at the lowest spins (i.e., γ-ray energies) in the collective bump component.[2] The option to cancel the discrete lines is not available in this dataset since we have not selected a specific final nucleus, and the intensities of the discrete lines shift with changing K values.

An example of how this analysis looks in the ^{48}Ca on ^{124}Sn reaction recorded with the 8PI spectrometer is shown in Fig. 6. These spectra are unprocessed, but this does not affect the point. We can extract a well-defined result for the average spectrum of new transitions entering at the top of the cascade in the figure associated with $K=24$. The normalizations chosen to zero the statisticals, or to zero the counts at the lowest spins in the collective bump region, say, $E_\gamma \approx 950-1050$ keV are closely equivalent, as can be seen in the inset in Fig. 6.

A more quantitative way to extract the information is to normalize the processed spectra to their associated multiplic-

[2]The feeding of the lowest spins in the collective bump component becomes saturated at some moderate entry spin, and should show no change in intensity with higher entry spins, for example, Ref. [12].

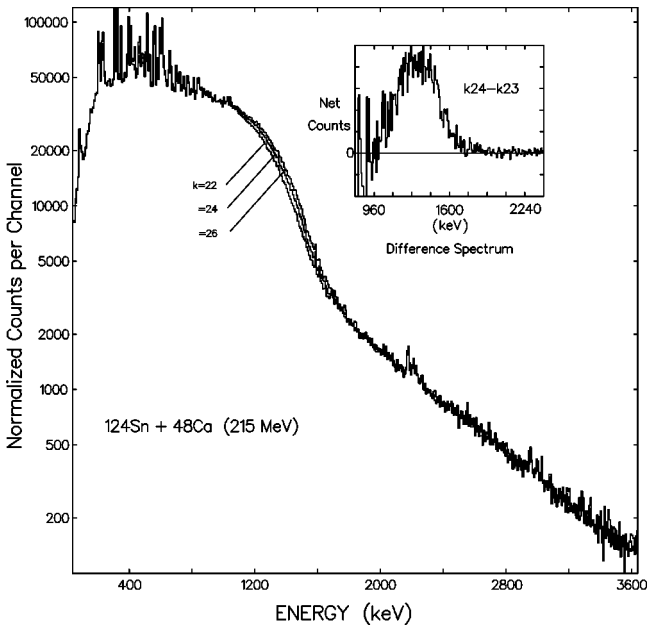

FIG. 6. Results with the 8PI spectrometer. Unprocessed spectra, gated on the K values shown, and normalized to the same number of counts in the statistical region of the spectrum ($E_\gamma \geqslant 2000$ keV). The same normalization also brings the counts at the lowest spins in the collective $E2$ bump, say $E_\gamma \approx 950-1050$ keV, to near equality. We conclude that either of these normalizations will produce similar results for the difference spectra at the peak of the collective $E2$ bump.

ity [12]. Following this procedure, the integral of the counts in the spectrum (after processing) is set equal to the multiplicity associated with the K value as defined in Sec. III D above. The subtraction of such normalized spectra results in a normalized spectrum by construction. We have chosen to subtract the lower member from the higher one for pairs of spectra gated on folds $K+1$ and $K-1$, or on folds K and $K-1$. Typical results are shown in Fig. 7. The $E2$ bump is evident in these results; its centroid is well defined and could be reliably determined. In order to compare the relative strengths of the $E2$ bumps in Fig. 7 we have scaled the difference spectra to an area corresponding to unit transition strength.

1. Precautions concerning the selection of high-spin states by K selection

For high counting rates, there can be pileup effects in the electronics such that two separate fusion events of average multiplicity are registered as one event of approximately double the average multiplicity. At the event rates maintained in these experiments, the effects were negligible within the K range processed.

For K selections near the end of the measured range, where there are very few states of higher spin to be selected, spurious effects will come into play. For example, a limit occurs when the population of increasingly higher-spin states falls more rapidly than the tail of a typical multiplicity response function of the instrument (such as shown in Fig. 1). This means that the instrument is incapable of resolving such

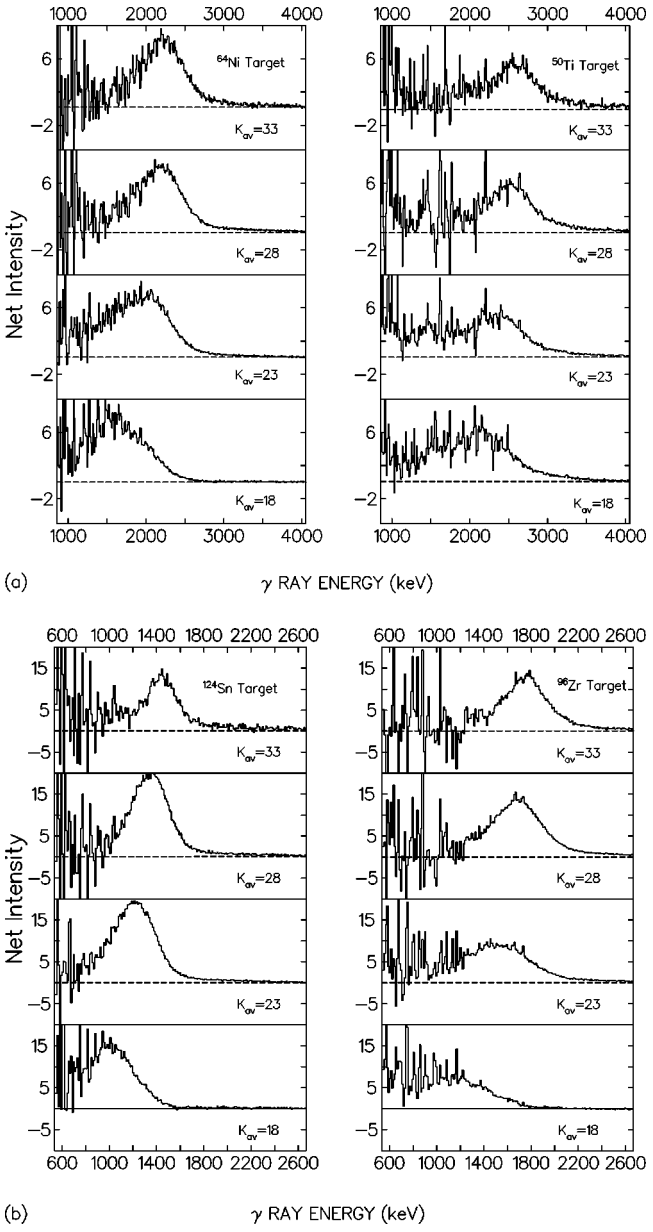

FIG. 7. Typical results for the incremental spectra. In each case, the processed and multiplicity-normalized spectra gated on folds $K-1$ have been subtracted from those gated on $K+1$. The value K_{av} is the midvalue of K. The spectra have been scaled so that their integral corresponds to unit transition intensity, i.e., to $M=1$.

weakly populated high-spin states, and the deconvolution of the K-spectrum should, in principle, show a saturation effect at some limiting M value.

An effect that shows up in simulations of the Gammasphere detector is that for K selections near the end of the measured range, there is a decreased peak-to-total response in the HPGe detectors. The effect arises because a suppression failure in Gammasphere can result in the triggering of an adjacent BGO module. Thus at some level, an increased number of hits can be generated by selecting events with an above-average number of suppression failures. The 8PI spectrometer is less sensitive to this problem because the BGO suppressors are not close packed.

Going beyond the response of the instrument, there can also be a spurious effect arising from branching in the nuclear level scheme. If we select events of increasing K, then, in principle, there must come a point where we begin to select decay paths with more than average multiplicity without increasing the spin. In the simulations of this effect, we find that for high-spin cascades, the instrumental limits described above will come into play before this particular spurious effect becomes measurable.

An experimental method to check that the instrument is truly selecting events of higher angular momentum with increasing K value is to note the relative populations of the various reaction channels derived from the discrete-line intensities. To be conservative, we have restricted the data shown here to K values for which the population was no less than 8% of the peak K population.[3] In this range, we found that as a function of K selection, the population of the highest-spin channel was always increasing relative to the channels of lower spin.

F. Centroids of the incremental γ spectra versus spin: Kinematic moments of inertia

We are now positioned to express the data in the form of plots of the energy centroids of the collective $E2$ bumps in the incremental spectra versus an associated angular momentum. Experimental values for the energy centroids of the incremental collective bumps were found to be robust, in the sense that they were insensitive to which of the procedures described in Sec. III E was adopted. The associated angular momenta were derived from the parametrization given in Table III. An indication of the spread arising from different experiments and from different analysis techniques is shown in Fig. 8. The shaded bands in Fig. 8 are intended to represent in an approximate way the uncertainty in the measured trends. In what follows we show only the shaded bands as representing the data. Figure 9 shows the same data plotted as spin versus rotational frequency. In addition, the solid lines give the results of a modified Thomas-Fermi model, which will be described in Sec. IV B 1 and compared with the experimental results in Sec. V.

From the γ-ray energy E_γ associated with the $E2$ transition between the states of spin $(I+1)$ and $(I-1)$ we may derive the kinematic moment of inertia as

$$\Im^{(1)}=\hbar^2(2I+1)/E_\gamma, \tag{6}$$

and these results are summarized in Fig. 10.

G. Widths of the collective bump in the incremental spectra

The observed widths of the incremental collective $E2$ bumps are summarized in Table IV. The spread in these γ-ray energies arises from (a) a spread in the moments of inertia and in the aligned spin in the feeding region (often called rotational damping) and (b) the spread in γ-ray multiplicity (angular momentum) selected by the instrument.

[3]Intensities as determined with the trigger bias.

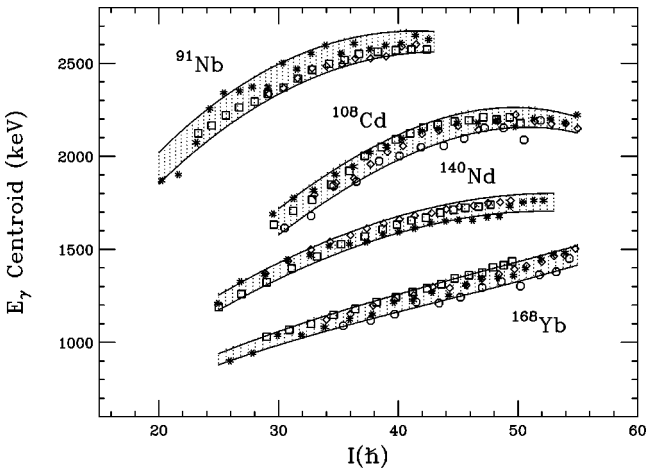

FIG. 8. Summary of collective $E2$-bump centroids and their associated spins. Circles refer to data sets taken with the 8PI spectrometer, other symbols refer to Gammasphere data with different analysis procedures as discussed in the text. The shaded area is intended to represent an envelope of the extremes of the experimental uncertainties, and further presentations of the data depict only the shaded region. Labels refer to each dominant reaction channel at high spin.

This latter effect would cause a spread in the collective $E2$ bump energies even in the case of a perfect rotor, where all of the bands had identical properties, so that $E\gamma(I)$ were uniquely related to spin. The instrumental broadening can be determined from experiment since the distribution functions $f_K(M)$ (Sec. III D) are known, and the collective bump centroid energies have been determined. Results for the instrumental contribution to the widths are shown in Table IV. Generally we conclude that the instrumental contribution is unimportant. Partly, this is because excepting the residues from reactions on the ^{124}Sn target, the γ-ray energies are more similar to spin than would be the case for a pure rotor. In fact, the trend of the centroid energies of the $E2$ bumps for given reaction partners to reach a near-constant value at

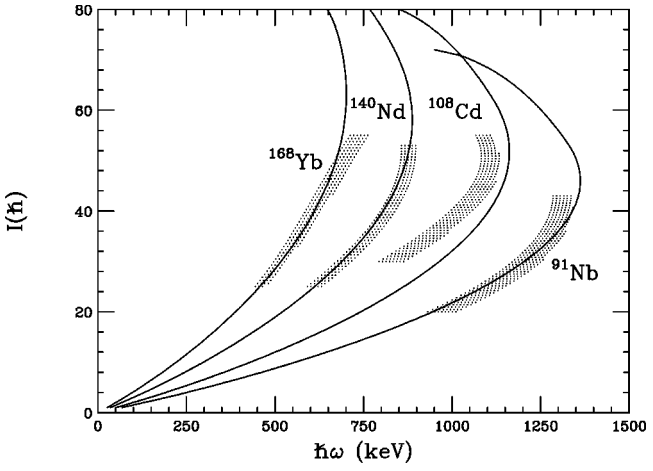

FIG. 9. Plots of the experimentally derived spin versus rotational frequency. The dynamical moment of inertia $\Im^{(2)}$ is given by the slope $dI/d\omega$. Solid lines indicate results of the modified Thomas-Fermi calculation discussed in Sec. IV B 1.

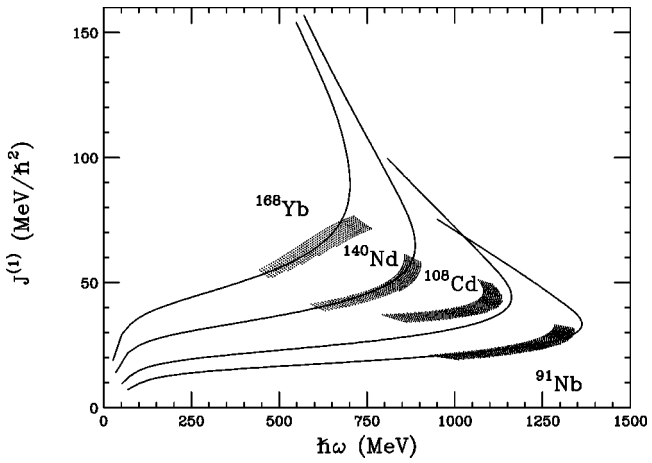

FIG. 10. Kinematic moments of inertia derived from the measured collective $E2$-bump centroids and their associated spins plotted against rotational frequency. The solid lines indicate results of the modified Thomas-Fermi calculation.

high spin (cf. Fig. 8), except in the case of the ^{124}Sn target, is reflected in the drop of the instrumental component of the bump width with spin, evident in Table IV.

It is interesting to consider whether the widths given in Table IV represent an upper bound on the magnitude of the damping width, usually denoted Γ_{rot}, or whether they are in fact the damping width. If the region of spin-excitation energy probed by the data were sufficiently far above yrast that it could be considered as a region where rotational damping were dominant, then the values in Table IV would be damping widths, and not just upper bounds. The value for the ^{124}Sn target (mainly ^{168}Yb residues with our high-K selection), $\Gamma_{rot}=280\pm50$ at spin $50\hbar$, is in good agreement with recent measurements for the damping width of the same system by Stephens *et al.* [13].

H. Intensities of the collective bump transitions

The intensity of the collective bump in the multiplicity-normalized incremental spectra does not account for the entire incremental spectrum; furthermore, we find that there is a systematic shift of the fractional strength exhausted by the collective bump, which varies with the mass of the residues. For angular momenta close to the experimental peak yields, the collective bump accounts for $85\%\pm7\%$ (^{124}Sn target), $70\%\pm7\%$ (^{96}Zr target), $58\%\pm10\%$ (^{64}Ni target), and $40\%\pm4\%$ (^{50}Ti target) of the incremental spectra. For higher angular momenta, corresponding to values beyond the quarter point of the multiplicity distributions shown in Fig. 5, the intensities may decrease, but this could be due to uncertainties in the multiplicity normalization for high multiplicities, where the deconvolution of the observed distributions from K to M begins to become problematic.[4]

These results of Sec. III are discussed in Sec. IV below.

TABLE IV. Analysis of the widths (full width at half maximum) of the collective $E2$ bump at selected spins.

Target	Spin	ΔE (keV) observed	ΔE (keV) contribution from ΔM	ΔE (keV) corrected
^{50}Ti	32	640(100)	200(30)	610(100)
	39	500(100)	120(30)	485(100)
^{64}Ni	39	800(150)	300(40)	740(150)
	49	600(100)	100(50)	590(100)
^{96}Zr	37	630(100)	315(40)	545(100)
	43	520(100)	140(30)	500(100)
	49	430(80)	120(30)	415(80)
^{124}Sn	41	380(50)	190(30)	330(50)
	50	330(50)	170(30)	280(50)

TABLE V. The derived kinematic moments of inertia compared with the rigid-sphere values and the corresponding axis ratios. The spin value corresponding to the moment of inertia is given in parentheses.

Target	$\mathcal{J}_0^{(1)}$ ($\hbar^2$ MeV^{-1})	$\mathcal{J}^{(1)}$ ($\hbar^2$ MeV^{-1})	Axis ratio
^{50}Ti	25.6	33.1 (43$\hbar$)	1.6
^{64}Ni	34.0	50.7 (55$\hbar$)	1.9
^{96}Zr	51.8	59.5 (52$\hbar$)	1.35
^{124}Sn	71.1	74 (55$\hbar$)	1.1

IV. DISCUSSION

A. Comparison with other experiments

The nuclear moment of inertia was investigated at very high spin by Folkmann *et al.* [14]. They studied the reactions ^{50}Ti+^{50}Ti and ^{50}Ti+^{110}Pd over a range of bombarding energies with a sum spectrometer. The ^{50}Ti target would produce residues in a similar range to the present experiment, and for that case (^{50}Ti+^{50}Ti) at the highest bombarding energy they found $2\mathcal{J}^{(1)}/\hbar^2=75\pm5$ MeV^{-1}, for $I\approx42\hbar$, which is 30% higher than the rigid sphere, and corresponds to an axis ratio close to 1.6:1. This result is in accordance with the present experiment (cf. Table V). For the ^{160}Er residues they found $2\mathcal{J}^{(1)}/\hbar^2=137\pm15$ MeV^{-1} for $I\approx42\hbar$, which is 5–15 % higher than the rigid sphere, and in approximate agreement with our value for ^{168}Yb if we allow for an $A^{5/3}$ dependence.

Similar experiments to determine $2\mathcal{J}^{(2)}$ values for isotopes of Er, Yb, Hf, and W were performed by Deleplanque *et al.* [15]. In all cases except for the tungsten isotopes, the $\mathcal{J}^{(2)}$ values rise above the rigid-sphere value beginning around $\hbar\omega=0.5$ MeV, and reach ≈1.4 to 1.6 times the rigid-sphere value by $\hbar\omega=0.7$ MeV, which is the highest frequency measured. In that experiment, the $\mathcal{J}^{(1)}$ values, specifically in ^{156}Er and ^{160}Er, were $\approx17\%$ higher than the rigid sphere. The closest point of comparison with the present experiment is for the ^{124}Sn target, leading to mainly ^{168}Yb at very high spins. In the present experiment for ^{168}Yb, the

[4]The deconvolution process will fail for the highest multiplicities, where the M spectrum of the reaction falls as rapidly as the instrumental response, cf. Fig. 1.

dynamical moment of inertia increases with rotational frequency, roughly in line with typical values measured for ^{162}Yb, ^{166}Yb, and ^{168}Hf in Ref. [15]. For example, comparing ^{166}Yb and ^{168}Yb in the two experiments the measured values rise approximately linearly from $\mathfrak{I}^{(2)}=70\hbar^2$ to $120\hbar^2$ MeV^{-1} as the rotational frequency goes from $\hbar\omega=0.5$ to 0.7 MeV.

The experiments of Macchiavelli *et al.* [16] measured with a sum spectrometer, the reactions of ^{40}Ar beams on six targets ranging from ^{50}Ti to ^{130}Te for bombarding energies in the range 170–185 MeV. Their results for ^{50}Ti and ^{68}Zn targets should correspond approximately with our own ^{50}Ti and ^{64}Ni targets. At low rotational frequencies, they found $\mathfrak{I}^{(2)}$ values close to the rigid sphere, but in the case of ^{50}Ti, ^{82}Se, ^{100}Mo, and ^{124}Sn targets, $\mathfrak{I}^{(2)}$ values increased to $\approx$50% greater than the rigid sphere at the highest rotational frequencies measured. This is not in accordance with our results, which indicate a much larger increase in $\mathfrak{I}^{(2)}$ values for the ^{50}Ti and ^{64}Ni targets over the same range of rotational frequency. For example, the $\mathfrak{I}^{(2)}$ values for the ^{50}Ti and ^{64}Ni targets diverge towards infinity for $\hbar\omega=1.3$ and 1.1 MeV, respectively, as can be seen from the vertical rise of $\mathfrak{I}^{(2)}$ in Fig. 9. Values for $\mathfrak{I}^{(1)}$ in those experiments [16] were derived both from determinations of the $E2$ bump centroid in difference spectra versus angular momentum, and by integrating the experimental $\mathfrak{I}^{(2)}$ values. These methods gave consistent results, and the derived $\mathfrak{I}^{(1)}$ values are rather close to the rigid sphere. Except for the case of our ^{124}Sn target, these results are not in agreement with the present experiment, as is evident in Table V.

A possible explanation for the discrepancy with Ref. [16] lies in the method they used to derive $\mathfrak{I}^{(2)}$ values. They used the relationship

$$2\,\mathfrak{I}^{(2)}/\hbar^2=8N_\gamma, \tag{7}$$

where N_γ is the number of rotational γ-ray transitions per unit energy bin derived from the multiplicity-normalized processed spectra. This formula is strictly applicable only to the transitions lying below the feeding region.[5] The procedure is valid where the states at high spin have a collective rotational character. This can be tested by noting whether or not the collective $E2$ bump accounts for all the intensity in the normalized incremental spectra as detailed in Sec. III H. In the present experiment, the collective $E2$ bump accounted for 85%$\pm$7% in the ^{124}Sn target (^{168}Yb residues), and this is probably generally true for the very collective rotors in that mass region. However, with the ^{64}Ni target (^{108}Cd residues), the collective $E2$ bump accounts for only 58% $\pm$10% of the spectrum, and clearly Eq. (7) will give $\mathfrak{I}^{(2)}$ values that are too small. As a check, we have analyzed our data with the procedures of Macchiavelli *et al.*, and indeed we can reproduce their results after scaling the $\mathfrak{I}^{(2)}$ values by $A^{5/3}$ to remove the (small) mass dependence.

[5]It can be extended into the feeding region using an analysis developed in Ref. [15].

B. The Jacobi transition

The signature of a fluid rotating in a Jacobi-like triaxial configuration is the decrease of rotational frequency with increasing angular momentum. This result is due to the rapid increase in the fluid's elongation (and moment of inertia) caused by the centrifugal force, once the Jacobi regime has been entered. A pedagogical paper on this has recently been published by Dankova and Rosensteel [17]. For classical fluids, the onset of the Jacobi regime is abrupt, with a discontinuous change in the sign of the slope in a plot of frequency versus angular momentum. This takes place at a critical angular momentum where the triaxial Jacobi-like configurations bifurcate from the family of McLaurin-like oblate shapes.

In nuclei, the frequency of collective rotation is directly related to the $E2$ γ-ray energy by $\hbar\omega\approx E_\gamma/2$. The Jacobi signature would thus be a systematic decrease of E_γ with increasing spin. This is expected to take place only for nuclei in a certain range of mass numbers and spins. As an estimate of this range, we note that for an idealized, incompressible, uniformly charged drop, the Jacobi regime is confined to not too highly charged systems, with a fissility parameter $x\leqslant 0.7315$, and with a rotational parameter y greater than $y_1(x)$, where [2]

$$y_1(x)=0.2829-0.3475x-0.0016x^2+0.0501x^3. \tag{8}$$

The fissility parameter x is a measure of the disruptive electrostatic forces, and is defined as the ratio of the electrostatic energy of the spherical liquid drop to twice its surface energy. The rotational parameter y is a measure of the disruptive centrifugal forces and is defined as the ratio of the rotational energy of a rigidly rotating spherical configuration to its surface energy.

In the nuclear case, the estimates[6]

$$x\approx(1/50)(Z^2/A) \tag{9}$$

and

$$y\approx 2I^2/A^{7/3} \tag{10}$$

in Eq. (8) allow an estimate of the angular momentum at the Jacobi point for nuclei idealized as liquid drops. The Thomas-Fermi theory provides a considerably more realistic description of the nucleus than does the liquid-drop model. It is a self-consistent, mean-field, semiclassical solution of the problem of nucleons interacting by finite-range effective forces that have been adjusted to reproduce accurately a wide range of static nuclear properties. The model has been generalized [18] to include a rotational energy corresponding to synchronous rotation.[7] With this idealization, the Jacobi regime again appears abruptly at a critical angular momentum

[6]More exact expressions for x and y may be found in Cohen *et al.* [2].

[7]In synchronous rotation it is assumed that all mass elements rotate with the same angular velocity—cf. Sec. VI B for a relaxation of this condition.

TABLE VI. Summary of the maximum angular momentum for fusion, L_{max}, the Jacobi transition angular momentum L_1, and the angular momentum for which the Jacobi fission barrier vanishes, L_2. Also shown is L_M, which is the angular momentum at which the maximum γ-ray energy is reached in the modified Thomas-Fermi theory.

Target	Incident energy (MeV)	L_{max} ($\hbar$)	L_1 ($\hbar$)	L_2 ($\hbar$)	L_M ($\hbar$)
^{50}Ti	200	70	56	75	46
^{64}Ni	207	79	62	82	52
^{96}Zr	207	86	72	90	57
^{124}Sn	215	88	76	85	64

$L_1(A,Z)$, a function of A and Z. Accurate algebraic formulas representing the numerically calculated properties of a rotating Thomas-Fermi nucleus with a given A, Z, and angular momentum L are given in the Appendix and in [19]. They include expressions for the energies $E_M(A,Z,L)$ and $E_J(A,Z,L)$ of the oblate Maclaurin configurations and the triaxial Jacobi shapes, as well as for the fission barrier heights of these rotating nuclei. In particular, equations are provided for the above-mentioned critical angular momentum $L_1(A,Z)$ and for the angular momentum $L_2(A,Z)$, where the fission barrier for the Jacobi shape vanishes (see Table VI).

In a classical approximation, the energy for a stretched quadrupole γ ray would be calculated by taking the difference

$$\gamma_L = E(L) - E(L-2) \approx 2(dE/dL)_{L-1} \tag{11}$$

or

$$\gamma_{L+1} \approx 2(dE/dL)_L . \tag{12}$$

These nominal γ-ray energies are to be compared with the experimental values E_γ, which are plotted in Fig. 11 as functions of L. The sharp change in slope at L_1+1 marks the transition of $E(L)$ to the Jacobi configurations at $L=L_1+1$, and the curves in Fig. 11 stop at L_2+1, where the fission barrier vanishes.

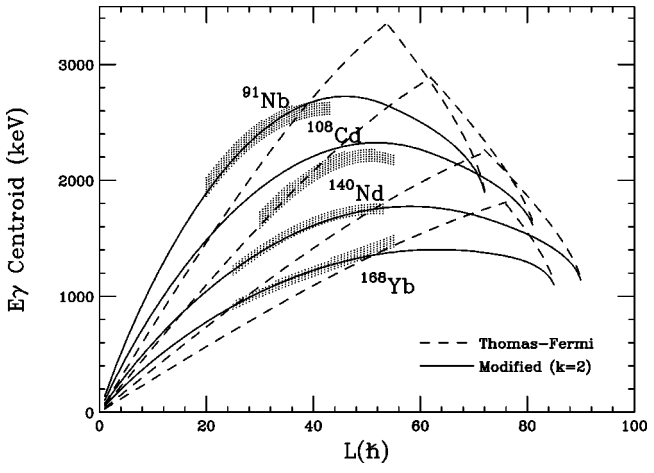

FIG. 11. Comparison of the measured collective $E2$-bump centroids versus spin with the Thomas-Fermi calculations, shown both without (dashed line) and with (solid line) the modifications described in the text.

In preparing this figure we assumed that the effective Z and A were those given by calculations with the statistical model code, EVAPOR [20]. These corresponded to the four-neutron evaporation channel except for the ^{50}Ti target, for which case $Z=41$, $N=50$ (^{91}Nb) was closest to the calculated centroid of the residue cross sections.

1. Modified Thomas-Fermi formulas

Hundreds of measured rotational spectra show that for low angular momenta, the energy $E(L)$ invariably rises more steeply than given by the Thomas-Fermi model as illustrated in Fig. 11. The implied effective moments of inertia are considerably lower than those corresponding to (rigid-body) synchronous rotation. This is associated with nuclear pairing and is expected to disappear with increasing values of L. In particular, in the regime of very deformed Jacobi shapes rotating about the shortest axis, the moment of inertia estimated assuming synchronous rotation should be accurate. We have accordingly modified the formula for $E(L)$ by interpolating between $1/k$ times the Thomas-Fermi formula for $E_M(L)$ for small L (where k is a number greater than unity, implying a moment of inertia that is less than rigid) and the Thomas-Fermi formula for $E_J(L)$ near $L=L_2$. The interpolation (detailed in the Appendix) is made with a curve that is smooth up to and including second derivatives, thus removing, by construction, the slope discontinuity apparent in the dashed curves in Fig. 11. This was done in recognition of the fact that collective nuclear rotations, also at low spin, are already associated with (mostly) prolate shapes. Hence, as the increasing angular momentum forces them into the Jacobi regime, one no longer expects a sharp transition caused by the breaking of axial symmetry about the rotation axis.

In these calculations, we have chosen a fixed scaling factor, $k=2.0$, for all the residues, and have not attempted to find the best individual fit to the experimental data for each nucleus. It should be noted that each interpolated curve $E(L)$ is constructed to pass through the point L_2 at the calculated excitation energy. It is readily verified that this implies that for any scaling factor k the integral under the interpolated curve γ_L for a particular residue is independent of k, and equal to that under the unmodified theoretical curve.

Our prescription that the modified and original energy curves in Fig. 12 come together at L_2 implies that the pairing energy, destroyed for small L, has been *restored* by the time the point L_2 is reached. The possibilty of such *pairing restoration* was discussed in Ref. [21], where it was shown that for a very deformed shape, particularly a necked-in shape, much of the total angular momentum is carried in what will become the orbital angular momentum of the two fragments, and relatively little is carried in intrinsic angular momentum of each fragment (relevant to destroying its pairing energy). In the most extreme case of a necked-in shape and complete pairing restoration, the energy of the configuration might even fall below the solid curve in Fig. 12, since now there are two fragments whose combined pairing energy could be

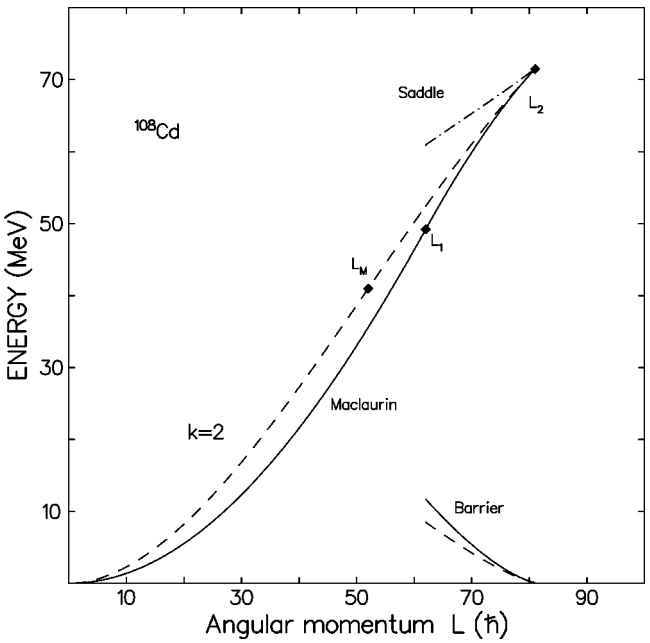

FIG. 12. The energy of synchronously rotating Thomas-Fermi nuclei as a function of angular momentum for ^{108}Cd (solid line) and with the modifications described in the text (dashed line). The start of the Jacobi regime of decreasing γ-ray energies with increasing spin is indicated by L_1 (or L_M in the modified theory). The point at which the fission barrier vanishes is indicated by L_2; by construction, this is the same in both treatments. The unmodified and modified heights of the fission barrier are plotted for L decreasing below L_2.

greater than that of the original nucleus. In view of these uncertainties, we have adopted the neutral prescription of simply joining the original and interpolated curves at the point L_2 rather than possibly introducing a second adjustable parameter to represent the energy of the modified curve at that point. At the most this prescription could introduce an error of the order of 3 MeV, and so change the area under the γ-ray curve E_γ in Fig. 11 by a few percent.

V. COMPARISON OF THEORY WITH THE DATA

Figure 11 shows the shaded regions representing the data from Fig. 8 juxtaposed with the unmodified Thomas-Fermi model (dashed) curves and with the modified (solid) curves. In the former case there is no correspondence between theory and experiment, showing that there is no evidence in the collective nuclear rotations studied here of a sudden transition from oblate to triaxial shapes. But after decreasing the low-spin moments of inertia (increasing the initial slopes of the solid curves in Fig. 11) and demanding a smooth interpolation towards the terminating Jacobi regime at high spin, the calculated curves follow the trends in the data. The correspondence is not perfect: the ^{108}Cd curve is 10% too high, and the ^{168}Yb curve has more curvature than the almost linear trend of the data. The latter may be due to a shell effect that has ''locked'' the nucleus into an almost fixed configuration in the range of spin observed, thereby preventing any significant centrifugal stretching that is responsible for the curvature of the calculated trend. By increasing the value of the parameter k the correspondence of theory with the ^{91}Nb and ^{140}Nd data could be improved, but other factors should be kept in mind. In particular, the curves are for a single residual nucleus, whereas in reality, there is a distribution of residues in each case, although we refer to each mixture by the name of the main product under our gating conditions. Moreover, the composition of the residues will depend on the angular momentum, with more particles evaporated at low spin than at high spin. The formulas in the Appendix can be used to investigate the effect of different assumptions.

A. Comparison of moments of inertia

In Fig. 11 we compared experiment and theory at the level of the γ-ray energy centroids. We can also make a comparison at the level of the kinematic moments of inertia, and this was shown in Fig. 10. The calculated curves terminate at the spin where the fission barrier for the Jacobi shape is calculated to vanish. In all four cases the interpolated calculation gives a fair representation of the variation of $\mathfrak{I}^{(1)}$ with spin, although the calculated absolute values for ^{108}Cd are $\approx$12–15 % too small. The increase in $\mathfrak{I}^{(1)}$ over the measured range of spins is $\approx$40% in both the experiment and theory.

At the highest spins measured, the observed kinematic moments of inertia are larger than those estimated for a rigid sphere, namely,

$$\mathfrak{I}_0^{(1)}/\hbar^2 \approx 0.0139 A^{5/3} \ \text{MeV}^{-1} \tag{13}$$

as detailed in Table V. To gain some insight into the deformation these moments of inertia might imply, we note that the moment of inertia of a prolate spheroid with semiaxes $a{:}a{:}c$ rotating about the a axis, divided by the moment of inertia of a sphere of equal volume and radius R is given by

$$\mathfrak{I}/\mathfrak{I}_0 = (a^2+c^2)/2R^2, \tag{14}$$

where

$$a^2 c = R^3. \tag{15}$$

The results for the derived axis ratios, c/a are given in Table V.

The dynamical moment of inertia $\mathfrak{I}^{(2)}$ is defined by

$$\mathfrak{I}^{(2)}/\hbar^2 = dI/(\hbar\, d\omega). \tag{16}$$

Figure 9 shows that except for the case of reactions on the ^{124}Sn target, there is a trend for continuously increasing slopes $dI/d\hbar\omega$ and hence $\mathfrak{I}^{(2)}$ values that continuously rise with rotational frequency. To facilitate comparison with other experiments, the $\mathfrak{I}^{(2)}$ values observed at the lowest spins are summarized in Table VII. At the highest spins for reactions on the ^{124}Sn target (essentially ^{168}Yb residues) we measure $\mathfrak{I}^{(2)}/\hbar^2 = 115 \pm 10$ MeV, which is in good agreement with the value given in Ref. [15] of 120 ± 10 MeV, after scaling ^{166}Yb to ^{168}Yb by $A^{5/3}$. The other reactions studied by us show essentially infinite values for $\mathfrak{I}^{(2)}/\hbar^2$ at the highest spins, as is apparent from the near-horizontal slopes in Fig. 8 and the near-vertical slopes in Fig. 9.

TABLE VII. The derived dynamical moments of inertia at the lowest spins measured.

Target	Spin	$\mathfrak{I}^{(2)}$ ($\hbar^2$ MeV^{-1})
^{50}Ti	$20\hbar$	33 ± 3
^{64}Ni	$30\hbar$	42 ± 3
^{96}Zr	$25\hbar$	55 ± 4
^{124}Sn	$25\hbar$	85 ± 4

B. Alignment gains at high spin

Large increases in the moment of inertia reflect changes in nuclear structure that may arise from increased deformation due to centrifugal effects, as discussed above, or due to changes in the occupation of specific orbitals. These effects are not necessarily independent, since in order for the nuclear deformation to increase, there must be corresponding changes in the occupation of particular orbitals associated with large elongations. Changes in orbital occupations are related to a microscopic description of the deformation changes, which we are describing macroscopically as a Jacobi effect.

Alignment gains from a crossing with the intruder orbital within the valence space are commonplace between spin $10\hbar$ to $20\hbar$ in nearly all deformed nuclei. At much higher rotational frequencies, there can be alignment gain from crossings of the intruder orbital in the next shell above the valence shell. At such high frequencies these would presumably be unpaired crossings.

We have applied an empirical two-band mixing calculation to test whether our data can be reproduced by any choice of parameters in such a model. We find that if one is free to choose the crossing frequencies, alignment gains, and interaction strengths, the data can be roughly reproduced over the critical region of near-constant γ-ray energy. To do this, the interaction strength has to be of the order of 2.5 MeV, and the gain in aligned spin must be about $5\hbar$ in the ^{91}Nb case and about $10\hbar$ in the other cases. The required crossing frequencies are shown in Table VIII. The interaction strength is large, and seems unrealistic; nevertheless, it could be viewed as a way of *mocking up* multiple-band crossings.

An explanation in terms of alignment gains could be more convincing if the parameters could be estimated. However it is difficult to see how this can be achieved in practice, since the deformation is a crucial ingredient, and as discussed above, it may be changing dramatically over the region of interest. Nevertheless, Macchiavelli *et al.* [16] have estimated the critical frequency for the crossing as $\hbar\omega_c = 41A^{-2/3}$ MeV for a spherical nucleus, and this should be an upper limit. Furthermore, since the spin of the intruder orbital is roughly $A^{1/3}\hbar$, a typical alignment gain will be $\sim 2A^{1/3}\hbar$. The data of Refs. [14–16], which cover the mass range $A\sim 80$–165, all show that the moment of inertia starts to rise at sufficiently high $\hbar\omega$, and indeed, the onset frequency scales as $A^{-2/3}$, but it occurs near $\hbar\omega\sim 0.5\hbar\omega_c$; the presently observed crossing frequencies are also a factor of 2 lower than the spherical estimate. The magnitude of the required gain in aligned spin is consistent with the simple scaling rule. The fact that the alignment gain happens earlier than the above estimate is not so surprising since it was an upper limit.

We note that the pronounced increases in the moments of inertia $\mathfrak{I}^{(2)}$ observed in this work and in the references given above, which might be expected to correspond with large alignment gains, in fact correspond to only moderate gains: typical values would be in the range $(5$–$10)\hbar$, which is compatible with the gain expected from the the higher intruder orbital. This follows from consideration that the experimental $\mathfrak{I}^{(2)}$ value is given by

$$\Delta i = \int (\mathfrak{I}^{(2)} - \mathfrak{I}_0^{(2)}) d\omega, \tag{17}$$

where $\mathfrak{I}_0^{(2)}$ is a chosen reference value.

C. Oblate states at very high spin?

For classical rotating liquids, the Jacobi transition marks a bifurcation between oblate and triaxial states. Thus nuclei in a liquid drop or in a Thomas-Fermi description [18] can rotate at low and moderate angular momenta about their oblate symmetry axis as described classically by McLaurin spheroids, e.g., Ref. [17]. This type of noncollective behavior in real nuclei is seen at low spin in several regions of the nuclear chart, such as in the $A\approx 150$ region near ^{147}Gd [22] and in the $A\approx 215$ region near ^{212}Rn [23]. It is due to the increasing alignment of individual high-K valence nucleons along the nuclear symmetry axis that their orbital motion tends to polarize the nucleus into an oblate shape. The exci-

TABLE VIII. Interpretation of the dynamical moments of inertia $\mathfrak{I}^{(2)}$ as effects of aligned spin in a schematic two-band mixing model. The estimates are those given in Ref. [16]. To reproduce the main feature of the data, i.e., the flattening of E_γ with increasing spin, the interaction strength in the model must be in the range of 2–3 MeV.

Target	Crossing frequency (kev) (empirical)	Crossing frequency (keV) (estimated)	Alignment gain ($\hbar$) (empirical)	Alignment gain ($\hbar$) (estimated)
^{50}Ti	1220	3021	5.0	7.4
^{64}Ni	1035	1854	10.0	9.5
^{96}Zr	825	1521	10.0	10.4
^{124}Sn	585	1347	10.0	11.0

tation energy along the yrast line in these nuclei is, on average, proportional to the square of the angular momentum over the range of spin involved, thus resembling a rotational band, but the sequence of γ-rays is irregular, and comprises dipole as well as quadrupole radiation. However, there is little experimental evidence that such oblate structures and their associated irregular γ-ray sequences exist at high spin.

There are, however, examples at moderate to high spin, of another type of behavior—prolate or prolate-triaxial bands evolving gradually with increase in spin to an oblate state which terminates the band. This occurs when the valence nucleons have gradually aligned all their spins with the rotation axis, the oblate symmetry axis, thus gradually changing through triaxial shapes towards oblateness and a noncollective terminating state. These structures have been reviewed by Afanasjev *et al.* [24]. The energies of the transitions in these bands tend to deviate from the rotational formula, particularly as termination is approached.

We can speculate that if noncollective oblate states lying far above the yrast line exist, and are populated at very high spins, then the associated continuous γ-spectrum would be featureless, and difficult to identify experimentally. Nevertheless, the presence of this radiation can be inferred from the multiplicity-normalized difference spectra. In cases where all of the normalized difference (incremental) spectrum is not concentrated in the $E2$-bump region (cf. Sec. III H), one may assume that the balance must lie in some featureless spectrum, possibly characteristic of noncollective oblate rotation. There is evidence in the $A \approx 160$ region that the $E2$ bump does in fact exhaust most of the normalized spectrum [15,25], but in lighter nuclei, there seems to be a substantial noncollective component.

D. Conclusions

Figure 8 shows that in three of the four cases studied (^{168}Yb is the exception) the plot of E_γ vs I flattens out at high angular momentum, suggesting the presence of a maximum. There is, however, no evidence for an abrupt change in slope as would be predicted by a synchronously rotating Thomas-Fermi (or liquid-drop) model, shown by the dashed curves. When the predictions of the Thomas-Fermi model are modified by taking account of the reduction of the moments of inertia at low angular momentum by a factor of 2, as well as by smoothing out by interpolating the slope discontinuity (due to the preexistence of prolate shapes at low spins), the theoretical curves show a fair correspondence with the measurements. In the model, the flattening of $E_\gamma(L)$ and the eventual downturn is due to centrifugal stretching expected for Jacobi-like configurations. Confirming this interpretation would require the determination of quadrupole moments, which is difficult on account of the anticipated extremely fast transitions and the continuous nature of the radiation. The model treats three of the five most important influences on nuclear structure at high spin, namely, centrifugal forces, Coulomb repulsion, and surface energy. Of the two left out, pairing and shell effects, the former should be of lesser importance at the high-spin values of interest, so that shell effects are the main missing consideration. They can indeed be important. The absence of a leveling-out of $E_\gamma(L)$ in the case of ^{168}Yb might be due to a shell effect, which locked this nucleus into an almost undeformable potential energy pocket in the range of angular momentum observed so far.

Our results suggest—without proving it—that nuclei with sufficiently large angular momenta may exhibit approximately the universal features of rotating fluids, first noted in 1834 in the context of idealized gravitating masses.

ACKNOWLEDGMENTS

We would like to express our gratitude to the crew and staff of ATLAS, and of the 88-Inch Cyclotron. This work has been supported by the U.S. DOE under Contract No. DE-AC03-76SF00098 (LBNL).

APPENDIX

1. Thomas-Fermi formulas

Guided by scaling rules valid in the liquid-drop model (which is a lowest-order approximation to the Thomas-Fermi model), as well as by universal rules associated with bifurcations and limiting points in families of equilibrium shapes, we have constructed formulas in terms of the atomic and mass numbers, Z and A, and the angular momentum L, which accurately represent the numerically calculated properties of a number of Thomas-Fermi nuclei from Se to Yb. These formulas, given below, can then be applied to neighboring nuclei, thus avoiding the need for a separate Thomas-Fermi calculation for each nucleus of interest. In the following, energies are in MeV, and angular momenta are in units of $\hbar$.

The critical angular momentum at which the Jacobi transition takes place is given by

$$L_1 = 0.060\,29 A^{7/6}(40.83-\zeta)^{1/2}, \tag{A1}$$

where the fissility parameter ζ is defined as

$$\zeta = Z^2/\{1-1.7826([A-2Z]/A)^2\}A. \tag{A2}$$

The angular momentum at which the fission barrier vanishes is

$$L_2 = 0.091\,08 A^{7/6}(36.34-\zeta)^{1/2}. \tag{A3}$$

The energy of the oblate (Maclaurin-like) equilibrium shapes with respect to a nonrotating ground state is

$$E_M(L) = \gamma_1 L_1(0.3\lambda^2 - 0.025\lambda^4), \tag{A4}$$

where

$$\gamma_1 = 6.2811([44.60-\zeta]/A)^{1/2} \tag{A5}$$

and

$$\lambda = L/L_1. \tag{A6}$$

The energy of Jacobi shapes, bounded by $L_1 \leqslant L \leqslant L_2$, is

$$E_J(L)=\gamma_1 L_1\{0.275+\tfrac{1}{2}\kappa[\Gamma_2(1-X)+\tfrac{1}{2}(1-\Gamma_2-\beta)(1-X^2)+\tfrac{2}{3}\beta(1-X^{3/2})]\}, \quad \text{(A7)}$$

where

$$\Gamma_2=0.6118[1-(\zeta/38.91)^2]^2/[1-(\zeta/33.49)^2], \quad \text{(A8)}$$

$$\beta=0.3078, \quad X=(L_2-L)/(L_2-L_1),$$

$$\text{and} \quad \kappa=(L_2/L_1)-1. \quad \text{(A9)}$$

The energy of saddle-point shapes for $L\leqslant L_2$ is

$$E_S(L)=E_J(L)+B_1X^{3/2}, \quad \text{(A10)}$$

where

$$B_1=(2/3)\gamma_1 L_1\beta\kappa. \quad \text{(A11)}$$

For $L_1\leqslant L\leqslant L_2$, the fission barrier for the Jacobi shapes is $B_1X^{3/2}$.

For $L\leqslant L_1$ the fission barrier for Maclaurin shapes is

$$B_M(L)=E_S(L)-E_M(L). \quad \text{(A12)}$$

In order to derive expressions for the γ-ray energies we define energy derivatives as

$$\gamma(L)\equiv 2dE(L)/dL, \quad \text{(A13)}$$

so that

$$\gamma_L\equiv\gamma(L-1) \quad \text{(A14)}$$

is an accurate approximation to a nominal quadrupole transition energy from the state L to the state $L-2$. For the Maclaurin shapes we have

$$\gamma_M(L)=\gamma_1(1.2\lambda-0.2\lambda^3), \quad \text{(A15)}$$

and for the Jacobi shapes with $L_1\leqslant L\leqslant L_2$ we find

$$\gamma_J(L)=\gamma_1[\Gamma_2+(1-\Gamma_2-\beta)X+\beta X^{1/2}]. \quad \text{(A16)}$$

For $L=L_1$ we have $\gamma_M(L_1)=\gamma_1$, and for $L=L_2$ we have $\gamma_J(L_2)=\gamma_1\Gamma_2$.

The above equations have been verified to represent accurately the numerical Thomas-Fermi solutions for nuclei with mass numbers A greater than ~ 70 and less than ~ 170, or equivalently, for fissilities ζ in the range 15.8 to 30.7. They may be adequate for A less than 70, but should not be used for A greater than about 170, or for ζ greater than about 30.7. The expression for $B_M(L)$ may not be reliable for L much below L_1.

2. Modified Thomas-Fermi formulas

As explained in Sec. IV B 1, we constructed modified formulas by interpolating the energy $E(L)$ between k times the low-L behavior of $E_M(L)$ and the equation for $E_J(L)$ near $L=L_2$, by smoothly joining at L_1 the two expressions

$$E_<=\gamma_1 L_1[0.3k\lambda^2-0.025\lambda^4-a\lambda^n] \quad \text{for } L\leqslant L_1 \quad \text{(A17)}$$

and

$$E_>=\gamma_1 L_1\{0.275+\tfrac{1}{2}\kappa[\Gamma_2(1-X)+(1/2)(1-\Gamma_2-\beta)\times(1-X^2)+(2/3)\beta(1-X^{3/2})+bX^2]\}$$
$$\text{for } L_1\leqslant L\leqslant L_2. \quad \text{(A18)}$$

For a given k value, the three quantities n,a,b are determined by the requirement of continuity of value, slope, and curvature at $L=L_1$ (cf. Sec. IV B 1). The theoretical γ-ray energies will now change gradually from increasing to decreasing functions of L, but we shall continue to refer to the regime of decreasing γ-ray energy as the Jacobi regime.

The above-mentioned requirements of continuity lead to the following formulas for n, a, and b

$$n=[-B+(B^2+4AC)^{1/2}]/2A, \quad \text{(A19)}$$

$$a=0.3A(k-1)/(2+n\kappa), \quad \text{(A20)}$$

$$b=na-0.6(k-1), \quad \text{(A21)}$$

where A, B, and C are given by

$$A=2(1+\kappa)=2L_2/L_1, \quad \text{(A22)}$$

$$B=(2/\kappa)-A-V\kappa, \quad \text{(A23)}$$

$$C=(4/\kappa)+2V, \quad \text{(A24)}$$

where

$$V=2+[1+(1-\Gamma_2-\beta/2)/0.6\kappa]/(k-1). \quad \text{(A25)}$$

Figure 12 illustrates the Thomas-Fermi and modified Thomas-Fermi energies and fission barriers in the case of ^{108}Cd. The k value was taken to be 2.

Formulas for the energy derivative functions $\gamma(L)$ related to the $E2$ γ-ray energies γ_L by Eq. (A14) are

$$\gamma_<(L)=2\gamma_1[0.6k\lambda-0.1\lambda^3-na\lambda^{n-1}] \quad \text{for } L\leqslant L_1 \quad \text{(A26)}$$

and

$$\gamma_>(L)=\gamma_1[\Gamma_2+(1-\Gamma_2-\beta)X+\beta X^{1/2}-2bX]$$
$$\text{for } L_1\leqslant L\leqslant L_2. \quad \text{(A27)}$$

Varying k in the range from zero to infinity results in a one-parameter family of interpolation functions for $\gamma(L)$. The choice of $k=2$ turns out to give an approximate correspondence with the measurements, as seen in Fig. 11.

[1] R. Beringer and W.J. Knox, Phys. Rev. **121**, 1195 (1961).
[2] S. Cohen, F. Plasil, and W.J. Swiatecki, Ann. Phys. (N.Y.) **82**, 557 (1974); A.J. Sierk, Phys. Rev. C **33**, 2039 (1986).
[3] W.J. Swiatecki, in *Proceedings of the International Colloquium on Drops and Bubbles*, edited by D.J. Collins, M.S. Plesset, and M.M. Saffren (California Institute of Technology and Jet Propulsion Laboratory, 1974), Vol. 1, p. 52.
[4] W.D. Myers and W.J. Swiatecki, Acta Phys. Pol. B **27**, 99 (1996); Nucl. Phys. **A612**, 249 (1997).
[5] A. Maj *et al.*, Acta Phys. Pol. B **32**, 2433 (2001).
[6] H.R. Andrews *et al.*, Proposal for a National Facility: The 8PI Spectrometer, AECL Report No. 8329, 1984.
[7] M. Jääskelainen *et al.*, Nucl. Instrum. Methods Phys. Res. **204**, 385 (1983).
[8] I.Y. Lee *et al.*, Nucl. Phys. **A520**, 641c (1990).
[9] J.P. Martin *et al.*, Nucl. Instrum. Methods Phys. Res. A **257**, 301 (1987).
[10] S. Sie *et al.*, Phys. Rev. Lett. **46**, 405 (1981).
[11] T. Yamazaki, Nucl. Data, Sect. A **3**, 1 (1967).
[12] R.M. Diamond and F.S. Stephens, Annu. Rev. Nucl. Part. Sci. **30**, 85 (1980).
[13] F.S. Stephens *et al.* (unpublished).
[14] F. Folkmann *et al.*, Nucl. Phys. **A361**, 242 (1981).
[15] M.A. Deleplanque *et al.*, Nucl. Phys. **A448**, 495 (1986).
[16] A.O. Macchiavelli *et al.*, Nucl. Phys. **A443**, 538 (1985).
[17] Ts. Dankova and G. Rosensteel, Am. J. Phys. **66**, 1095 (1998).
[18] W.D. Myers and W.J. Swiatecki, Nucl. Phys. **A601**, 141 (1996).
[19] W.D. Myers and W.J. Swiatecki, Acta Phys. Pol. B **32**, 1033 (2001), available at ftp:/www-nsdth.lbl.gov/pub/myers/zak20
[20] EVAPOR, a Monte Carlo evaporation code by N.G. Nicolis (Washington University, St Louis) and J.R. Beene (Oak Ridge National Laboratory).
[21] W.D. Myers and W.J. Swiatecki, Nucl. Phys. **A641**, 203 (1998).
[22] B. Haas *et al.*, Nucl. Phys. **A362**, 254 (1981).
[23] D. Horn *et al.*, Nucl. Phys. **A317**, 520 (1979).
[24] A.V. Afanasjev *et al.*, Phys. Rep. **332**, 1 (1999).
[25] M.A. Deleplanque *et al.*, Phys. Rev. Lett. **43**, 1001 (1979).